Observational Constraints on Southern Ocean Cloud-Phase Feedback

Wall, C. J., Storelvmo, T., Norris, J. R. & Tan, I.

Published in: Jounral of Climate
DOI: 10.1175/JCLI-D-21-0812.1

Available online: 19 Jan 2022

Citation:
Wall, C. J., Storelvmo, T., Norris, J. R. & Tan, I. (2022). Observational Constraints on Southern Ocean Cloud-Phase Feedback. Journal of Climate, 35(15), 5087-5102. doi: 10.1175/JCLI-D-21-0812.1

Observational Constraints on Southern Ocean Cloud-Phase Feedback

CASEY J. WALL,[a] TRUDE STORELVMO,[b,c] JOEL R. NORRIS,[a] AND IVY TAN[d]

[a] *Scripps Institution of Oceanography, University of California San Diego, La Jolla, California*
[b] *Department of Geosciences, University of Oslo, Oslo, Norway*
[c] *School of Business, Nord University, Bodø, Norway*
[d] *Department of Atmospheric and Oceanic Sciences, McGill University, Montreal, Canada*

(Manuscript received 15 October 2021, in final form 19 January 2022)

ABSTRACT: Shortwave radiative feedbacks from Southern Ocean clouds are a major source of uncertainty in climate projections. Much of this uncertainty arises from changes in cloud scattering properties and lifetimes that are caused by changes in cloud thermodynamic phase. Here we use satellite observations to infer the scattering component of the cloud-phase feedback mechanism and determine its relative importance by comparing it with an estimate of the overall temperature-driven cloud feedback. The overall feedback is dominated by an optical thinning of low-level clouds. In contrast, the scattering component of cloud-phase feedback is an order of magnitude smaller and is primarily confined to free-tropospheric clouds. The small magnitude of this feedback component is a consequence of counteracting changes in albedo from cloud optical thickening and enhanced forward scattering by cloud particles. These results indicate that shortwave cloud feedback is likely positive over the Southern Ocean and that changes in cloud scattering properties arising from phase changes make a small contribution to the overall feedback. The feedback constraints shift the projected 66% confidence range for the global equilibrium temperature response to doubling atmospheric CO_2 by about +0.1 K relative to a recent consensus estimate of cloud feedback.

SIGNIFICANCE STATEMENT: Understanding how clouds respond to global warming is a key challenge of climate science. One particularly uncertain aspect of the cloud response involves a conversion of ice particles to liquid droplets in extratropical clouds. Here we use satellite data to infer how cloud-phase conversions affect climate by changing cloud albedo. We find that ice-to-liquid conversions increase cloud optical thickness and shift the scattering angles of cloud particles toward the forward direction. These changes in optical properties have offsetting effects on cloud albedo. This finding provides new insight about how changes in cloud phase affect climate change.

KEYWORDS: Climate sensitivity; Cloud microphysics; Cloud radiative effects; Feedback; Shortwave radiation

1. Introduction

The Southern Ocean is one of the cloudiest places on Earth. Vast blankets of low clouds cover the region, and streaks of high clouds form from the continuous churning of weather systems. Collectively these clouds have large radiative effects that shape global climate (Hwang and Frierson 2013; Kay et al. 2016; Hawcroft et al. 2017).

Southern Ocean clouds are also susceptible to producing cloud–climate feedbacks that have global consequences. For instance, projections from phase 6 of the Coupled Model Intercomparison Project (CMIP6) predict more positive Southern Ocean cloud feedback and higher climate sensitivity than previous assessments (Zelinka et al. 2020). The CMIP6 projections show that Southern Ocean cloud feedback affects climate sensitivity, but the models have large parametric uncertainties that cause them to predict a wide range of feedback values. Previous observational studies have attempted to constrain the feedback, but they have yet to reach a consensus on sign (Ceppi et al. 2016b; Terai et al. 2016; Lutsko et al. 2021). These results indicate that Southern Ocean clouds exert a potentially powerful but highly uncertain feedback on global climate change.

One major component of the feedback uncertainty is associated with changes in cloud thermodynamic phase (Storelvmo et al. 2015). As the atmosphere warms, some cloud particles that would have previously been ice will form as liquid instead. These phase conversions change shortwave (SW) cloud radiative effects in three primary ways. First, liquid droplets are typically smaller and more numerous than ice particles, so ice-to-liquid conversions increase cloud optical depth. Second, phase conversions change the shape of cloud particles, which changes the typical scattering angles of individual scattering events (Kokhanovsky 2004). Third, ice-to-liquid conversions may reduce precipitation efficiency, thereby extending cloud lifetimes and increasing cloud amount (Mitchell et al. 1989; Tsushima et al. 2006; Mülmenstädt et al. 2021). We refer to these changes in cloud scattering properties and lifetimes as the scattering and lifetime components of cloud-phase feedback, respectively. Both are the product of complex interactions among microphysical,

Denotes content that is immediately available upon publication as open access.

Supplemental information related to this paper is available at the Journals Online website: https://doi.org/10.1175/JCLI-D-21-0812.s1.

Corresponding author: Casey J. Wall, cawall@ucsd.edu

DOI: 10.1175/JCLI-D-21-0812.1

radiative, and dynamical processes, and thus they are highly uncertain.

In this study we use satellite observations to constrain the scattering component of Southern Ocean cloud-phase feedback. We focus on this feedback component because model simulations suggest that it could have a powerful stabilizing effect on climate (Ceppi et al. 2016a; Tan et al. 2016; Frey and Kay 2018), but observational evidence for the feedback has been limited to estimates that do not quantify confidence intervals or determine its importance relative to the overall cloud feedback (McCoy et al. 2014b; Tan et al. 2019). Here we introduce a method to estimate cloud feedback as a function of cloud-top phase, which facilitates stronger constraints. We first estimate the cloud-phase scattering feedback and the overall temperature-driven cloud feedback, and then we investigate the implications of these feedbacks for climate sensitivity.

2. Data and methods

a. Observations and model output

We extend a method of cloud-feedback analysis developed by Zelinka et al. (2012) to decompose SW feedbacks based on cloud thermodynamic phase. The method is applied to cloud observations from the Moderate Resolution Imaging Spectroradiometer (MODIS) instrument on the *Aqua* satellite (Platnick et al. 2017). MODIS cloud-phase data represent phase at cloud top, and they have a ~90% frequency of agreement with cloud-top phase determined by lidar, which is the most accurate phase retrieval from space. The frequency of agreement with lidar over the Southern Ocean is similar when considering single-layer clouds or single- and multilayer clouds combined (Huang et al. 2016; Marchant et al. 2016). We analyze MODIS cloud-fraction histograms partitioned by cloud-top pressure (CTP), optical depth, and phase. MODIS does not retrieve all of these properties when the solar zenith angle is larger than 81.4°, so the histograms are compiled from pixels that have solar zenith angle smaller than this value. Furthermore, the standard liquid- and ice-cloud histograms have different CTP-optical depth bins, so some adjacent bins are merged to make the intervals similar. The method for merging bins is described in Table S1 in the online supplemental material. All of the MODIS data are provided on a space–time grid with resolution of 1° latitude, 1° longitude, and 1 month.

We also use monthly gridded meteorological data and sea-ice area fraction from the ERA5 (Hersbach et al. 2020). Three-dimensional temperature, horizontal wind, and vertical wind fields are linearly interpolated to the MODIS grid and averaged over pressure intervals that correspond to the MODIS CTP bins. We also calculate estimated inversion strength, which represents the inversion at the top of the planetary boundary layer (Wood and Bretherton 2006). The observations and reanalysis data are analyzed over ocean grid boxes with monthly sea-ice cover below 1% to avoid biases in the MODIS data that occur over sea ice (Liu et al. 2010). We refer to these grid boxes as "ice-free ocean." Data are analyzed between the years of 2003 and 2019, and the main analysis is performed over latitudes of 40°–60°S. Unless stated otherwise, all analysis is performed over this latitude range.

Finally, we use output from 34 CMIP6 global climate models to represent CO_2-forced warming (Table S2). Model simulations are run for 150 years following an abrupt quadrupling of atmospheric CO_2 concentrations relative to preindustrial values (the abrupt4xCO2 experiment). Like the reanalysis data, atmospheric temperatures from the model output are interpolated to the MODIS grid and averaged over pressure intervals that correspond to the MODIS CTP bins. The temperature response to increasing atmospheric CO_2 is calculated by taking the difference between the abrupt4xCO2 simulation the corresponding parallel preindustrial simulation (the piControl experiment). The response of global-mean near-surface air temperature is calculated similarly. Only the first ensemble member from each model is used.

b. Radiative kernels

Cloud-fraction anomalies from each MODIS histogram bin are converted into top-of-atmosphere SW flux anomalies using radiative kernels. The kernels represent how much a unit cloud-fraction change modifies top-of-atmosphere SW flux with all noncloud factors fixed at climatological values. We calculate the kernels following the method of Zelinka et al. (2012), except that we generalize their framework by calculating separate kernels for liquid and ice clouds. The method for calculating the kernels involves performing radiative transfer calculations for an overcast cloud with various combinations of CTP, optical depth, and phase that correspond to the MODIS histogram bins. The liquid- and ice-cloud kernels are calculated with clouds that are entirely liquid and entirely ice, respectively. The calculations are performed using the Rapid Radiative Transfer Model for Global Climate Models (Clough et al. 2005) with the cloud optical property schemes of Fu (1996) and Hu and Stamnes (1993). We run the calculations with climatological seasonal cycles of humidity from ERA5 and surface albedo from Clouds and the Earth's Radiant Energy System satellite observations (Loeb et al. 2018). We also change the mean effective radius of liquid droplets and ice crystals to 14 and 35 μm, respectively, to match observed values over the Southern Ocean (McCoy et al. 2014a). Together the cloud histograms and kernels reproduce observed variations of SW cloud radiative effects with a bias of ~5% (appendix A).

Figure 1 shows the spatial and temporal average of the cloud histograms and radiative kernels over the Southern Ocean. The kernels have negative values because a larger cloud fraction increases SW reflection to space. They depend relatively strongly on optical depth, and they depend weakly on CTP because of SW absorption by water vapor above cloud top. For a given CTP–optical depth combination, the kernels also depend on cloud phase because ice particles typically backscatter more radiation than liquid droplets (Stackhouse and Stephens 1991). Changes in any of these cloud properties can therefore contribute to cloud feedback.

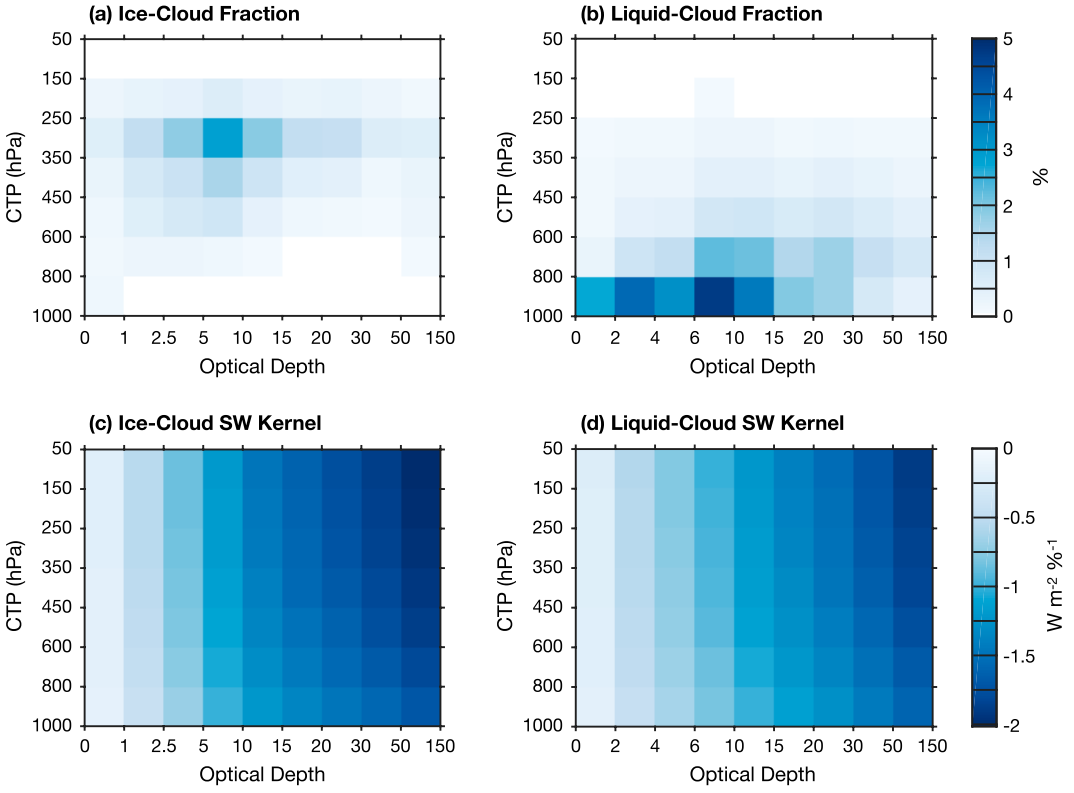

FIG. 1. Climatology of cloud fraction and SW cloud radiative kernels over the Southern Ocean: (a),(b) ice- and liquid-cloud fraction, and (c),(d) ice- and liquid-cloud kernels.

c. *Feedback analysis*

We leverage the MODIS histograms and kernels to estimate the component of SW cloud feedback that is directly caused by atmospheric warming. The analysis therefore does not include feedbacks from changes in large-scale circulation, horizontal advection over surface-temperature gradients, estimated inversion strength, or other meteorological factors that are not directly linked to local air temperature. We focus on temperature-driven feedbacks because most proposed mechanisms of extratropical cloud feedback are directly caused by atmospheric warming and because shifts in large-scale circulation are expected to produce a relatively small SW cloud feedback over the Southern Ocean (Terai et al. 2019; Ceppi and Hartmann 2015). Let i represent any bin in the MODIS liquid- or ice-cloud histogram. For a given location and calendar month, the SW feedback from clouds in bin i is

$$F_{\mathrm{SW},i} = \frac{\partial c_i}{\partial T_i} K_i \frac{dT_i}{dT_{2\mathrm{m}}}, \tag{1}$$

where c_i is cloud fraction, T_i is temperature at the location and pressure level of bin i, K_i is the corresponding element of the kernel, and $T_{2\mathrm{m}}$ is global-mean surface air temperature. On the right side of Eq. (1), the first term is the cloud response to local warming, the second term converts the cloud response into top-of-atmosphere SW flux, and the third term relates local warming to global-mean surface warming. All temperature-dependent terms represent the response to an external climate forcing. The task of quantifying cloud feedback thus reduces to estimating these terms.

We first calculate $dT_i/dT_{2\mathrm{m}}$, which represents the magnitude and vertical structure of atmospheric warming over the Southern Ocean relative to global-mean surface warming. This term is estimated by calculating temperature differences between the abrupt4xCO2 and piControl experiments of the CMIP6 models averaged over years 121–150 of the simulations. Values of $dT_i/dT_{2\mathrm{m}}$ are zonally averaged over ocean for each combination of latitude, calendar month, and pressure interval. We calculate $dT_i/dT_{2\mathrm{m}}$ for each of the 34 climate models, and we use the multimodel mean as the central estimate for the feedback analysis. The spatial- and annual-mean values of $dT_i/dT_{2\mathrm{m}}$ over the Southern Ocean consistently have maximum values in the free troposphere and smaller values in the lower stratosphere and near the surface (Fig. 2). Small stratospheric values are a consequence of larger emissivity from enhanced CO_2 concentrations, and small near-surface values are a consequence of ocean heat uptake and transport that result from the overturning circulation of the Southern Ocean (Hartmann 2016; Armour et al. 2016). These physical explanations and the consistency among models suggest that the projections of $dT_i/dT_{2\mathrm{m}}$ are robust.

The feedback analysis also requires radiative kernels for diagnosing feedbacks over ocean. Because the mean surface albedo has little zonal variation over ice-free ocean, we

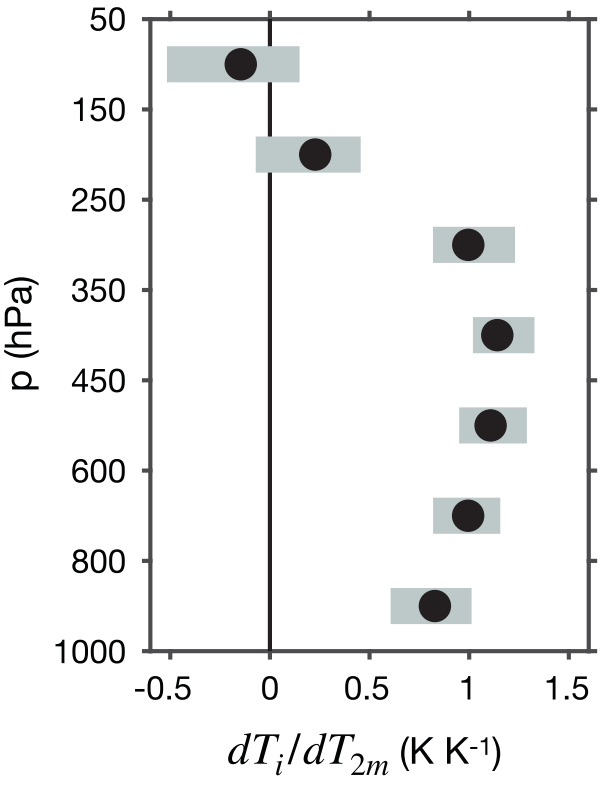

FIG. 2. Ratio of atmospheric warming over the Southern Ocean to global-mean surface warming from CMIP6 projections forced by a quadrupling of atmospheric CO_2 concentrations (dT_i/dT_{2m}). The plot shows spatial- and annual-mean values of dT_i/dT_{2m} over the Southern Ocean. Black dots show the multimodel mean, and gray bars show the intermodel range.

zonally average the kernels over these grid points. The resulting zonal-mean kernels are used in the analysis.

The remaining term in the feedback equation is $\partial c_i/\partial T_i$. This term represents the temperature-driven cloud response to a climate forcing, but it can be estimated from observed natural variability assuming that cloud–temperature relationships will not substantially change as the climate evolves. This assumption neglects the potential dependence of extratropical cloud feedbacks on the climate state (Bjordal et al. 2020). However, model projections generally suggest that monthly cloud–temperature relationships from natural variability accurately predict extratropical cloud feedbacks associated with anthropogenic climate change, and observed cloud–temperature relationships are similar in different epochs within the MODIS record (appendix C; Tselioudis et al. 1998; Gordon and Klein 2014; Terai et al. 2016; Ceppi et al. 2016b). We therefore estimate $\partial c_i/\partial T_i$ from observed natural variability.

We first estimate $\partial c_i/\partial T_i$ values associated with the combined effect of all feedback mechanisms that are directly caused by atmospheric warming. We call this the temperature-mediated cloud feedback, and we estimate the $\partial c_i/\partial T_i$ values by applying multilinear regression to the MODIS cloud histograms and reanalysis meteorological data over ice-free ocean. Because of the zonal symmetry of the Southern Ocean, regression is performed on data from all longitude points simultaneously. The climatological seasonal cycle is removed from each latitude–longitude grid box, and data are binned by latitude and calendar month. For each combination of latitude, calendar month, and histogram bin i, we calculate a regression model of the form

$$c_i = \sum_{n=1}^{N} \frac{\partial c_i}{\partial x_n} x_n + \epsilon, \tag{2}$$

where x_n are meteorological predictors, $\partial c_i/\partial x_n$ are regression coefficients, N is the number of meteorological predictors, and ϵ is the residual. The meteorological predictors include temperature and zonal, meridional, and vertical wind averaged over the pressure interval of bin i. Estimated inversion strength is also used as a predictor for bins with CTP $>$ 450 hPa. The term $\partial c_i/\partial T_i$ therefore represents the cloud response to local warming while the monthly wind field and inversion strength are held constant. On average, the regression model explains 37% of the variance of cloud-induced SW flux anomalies for boundary layer clouds (CTP $>$ 800 hPa) and 18% of the variance for tropopause-level clouds (250 $<$ CTP $\leq$ 350 hPa). The explained variance for boundary layer clouds is similar to that of other observational work that uses different meteorological predictors (Scott et al. 2020). This suggests that the regression model represents cloud–meteorology relationships with skill that is similar to other available methods. Ultimately the $\partial c_i/\partial T_i$ values are used to estimate the temperature-mediated cloud feedback following Eq. (1).

We also estimate the component of the temperature-mediated feedback that arises from changes in low-cloud optical depth. We define low clouds by CTP $>$ 600 hPa, and we use the method of Scott et al. (2020) to decompose anomalies in low-cloud fraction into a component associated with anomalous cloud amount and a component associated with anomalous shifts in the distribution of optical depth, phase, and CTP. Let L represent the total low-cloud fraction and c_j^* represent the cloud-fraction anomaly in histogram bin j that is associated with shifts in the optical depth–phase–CTP distribution. Values of c_j^* are determined by

$$c_j^* = c_j' - L' \frac{\overline{c_j}}{\overline{L}},$$

where j runs over all histogram bins with CTP $>$ 600 hPa, overbars indicate values from the climatological seasonal cycle, and primes indicate monthly anomalies. We regress c_j^* on monthly anomalies of the meteorological predictors to estimate the associated SW feedback. This feedback component is dominated by shifts in optical depth, so we henceforth call it the low-cloud optical depth feedback.

The values of $\partial c_i/\partial T_i$ associated with the scattering component of cloud-phase feedback are estimated from a different procedure. We calculate these terms separately for each combination of latitude, calendar month, and CTP bin so that phase conversions happen between clouds at the same latitude and pressure level. For a given CTP bin, the total liquid-cloud

fraction C_{liq} and the total ice-cloud fraction C_{ice} are calculated by summing cloud fraction over the optical depth dimension of the histogram. The proportion of clouds that are liquid is determined by

$$P_{\mathrm{liq}} = \frac{C_{\mathrm{liq}}}{C_{\mathrm{liq}} + C_{\mathrm{ice}}}.$$

We calculate P_{liq} for all data points that satisfy the given latitude–month–CTP combination, and we remove the climatological seasonal cycle from each latitude–longitude grid box. Monthly anomalies of P_{liq} are then regressed on monthly anomalies of the meteorological predictors to calculate $\partial P_{\mathrm{liq}}/\partial T$, where T is temperature in the CTP interval. Regression is performed on data from all longitude points simultaneously. Changes in C_{liq} and C_{ice} with warming are then determined by

$$\frac{\partial C_{\mathrm{liq}}}{\partial T} = \frac{\partial P_{\mathrm{liq}}}{\partial T}\langle C_{\mathrm{liq}} + C_{\mathrm{ice}}\rangle,$$

$$\frac{\partial C_{\mathrm{ice}}}{\partial T} = -\frac{\partial P_{\mathrm{liq}}}{\partial T}\langle C_{\mathrm{liq}} + C_{\mathrm{ice}}\rangle,$$

where angle brackets indicate values from the climatological seasonal cycle that are zonally averaged over ice-free ocean. The values of $\partial C_{\mathrm{liq}}/\partial T$ and $\partial C_{\mathrm{ice}}/\partial T$ are equal and opposite, so they represent a phase conversion with fixed overall cloud fraction. These values are distributed among the optical depth bins in proportion to the climatological distributions:

$$\frac{\partial c_{\mathrm{liq},k}}{\partial T} = \frac{\partial C_{\mathrm{liq}}}{\partial T}\frac{\langle c_{\mathrm{liq},k}\rangle}{\langle C_{\mathrm{liq}}\rangle},$$

$$\frac{\partial c_{\mathrm{ice},l}}{\partial T} = \frac{\partial C_{\mathrm{ice}}}{\partial T}\frac{\langle c_{\mathrm{ice},l}\rangle}{\langle C_{\mathrm{ice}}\rangle},$$

where $c_{\mathrm{liq},k}$ and $c_{\mathrm{ice},l}$ are the liquid- and ice-cloud fractions in optical depth bins k and l of the given CTP interval, respectively. By distributing cloud fraction this way, we are assuming that for any joint latitude–month–CTP bin, all ice clouds in the bin have the same probability of undergoing a phase conversion. Ultimately $\partial c_{\mathrm{liq},k}/\partial T$ and $\partial c_{\mathrm{ice},l}/\partial T$ are used to estimate the cloud-phase scattering feedback following Eq. (1). An example of this procedure is presented in the online supplemental material.

The cloud-phase scattering feedback is also decomposed into contributions from changes in different optical properties. The total cloud-phase scattering feedback for a given latitude, month, and CTP bin is

$$F_{\mathrm{SW,phase}} = \frac{dT}{dT_{2\mathrm{m}}}\left(\sum_{l=1}^{9}\frac{\partial c_{\mathrm{ice},l}}{\partial T}K_{\mathrm{ice},l} + \sum_{k=1}^{9}\frac{\partial c_{\mathrm{liq},k}}{\partial T}K_{\mathrm{liq},k}\right),$$

where K_{ice} and K_{liq} are the ice- and liquid-cloud kernels and the sums are performed over the optical depth dimension. Let $\hat{K}_{\mathrm{liq}}$ represent the liquid-cloud kernel evaluated on the ice-cloud optical depth bins. The feedback can then be expressed as

$$F_{\mathrm{SW,phase}} = \left[\frac{dT}{dT_{2\mathrm{m}}}\sum_{l=1}^{9}\frac{\partial c_{\mathrm{ice},l}}{\partial T}\left(K_{\mathrm{ice},l} - \hat{K}_{\mathrm{liq},l}\right)\right] + \left[\frac{dT}{dT_{2\mathrm{m}}}\left(\sum_{l=1}^{9}\frac{\partial c_{\mathrm{ice},l}}{\partial T}\hat{K}_{\mathrm{liq},l} + \sum_{k=1}^{9}\frac{\partial c_{\mathrm{liq},k}}{\partial T}K_{\mathrm{liq},k}\right)\right].$$

The first term in square brackets depends on the difference between the liquid- and ice-cloud kernels. This term represents the fact that converting ice to liquid without changing cloud optical depth will produce a feedback by changing the scattering angles of cloud particles and the relative importance of scattering and absorption. These optical properties are represented by the asymmetry parameter and single-scattering albedo, respectively. The second term in square brackets depends on the sum of $\partial c_{\mathrm{ice},l}/\partial T$ and $\partial c_{\mathrm{liq},k}/\partial T$ weighted by the liquid-cloud kernels. Since $\partial c_{\mathrm{ice},l}/\partial T$ and $\partial c_{\mathrm{liq},k}/\partial T$ have opposite sign and sum to zero when adding over all optical depth bins, this term represents the feedback from changes in the overall optical depth distribution that are caused by phase conversions.

All of the main feedback analysis is performed over ice-free ocean between 40° and 60°S. In some cases we perform additional calculations over different latitude ranges to facilitate comparisons with previous studies. These cases are explicitly identified in the text. Feedbacks are first calculated separately for each combination of latitude and calendar month. To ensure adequate sampling of the cloud histograms, we require that each grid box has at least 500 valid MODIS pixels. This condition is not satisfied poleward of 56°S in June and poleward of 59°S in July because of large solar zenith angles. In these cases, regression slopes are taken from the same latitude and the closest calendar month with sufficient data. If two months are equally close, then the average of their regression slopes is used. After these substitutions are made, the resulting feedback values are averaged over the seasonal cycle and latitude, weighting by the area of ice-free ocean. Feedback uncertainty is represented by 95% confidence intervals that account for uncertainty in observed cloud-temperature regression slopes, uncertainty in the cloud microphysical properties that are assumed when calculating the kernels, and intermodel spread in projections of $dT_i/dT_{2\mathrm{m}}$ (appendix B).

3. Southern Ocean cloud feedback

We next investigate the relative importance of the cloud-phase scattering feedback by comparing it with the overall temperature-mediated cloud feedback over the Southern Ocean. Figure 3 shows the feedback components as a function of CTP, optical depth, and phase. The temperature-mediated feedback includes a vertical dipole pattern from rising upper-tropospheric ice clouds (Fig. 3a). This is qualitatively consistent with established energetic constraints: The average depth of the troposphere is limited to levels with appreciable clear-sky radiative cooling, which is constrained to temperatures warmer than ~220 K by the nature of emission at wavelengths in the water-vapor rotation band (Hartmann and Larson

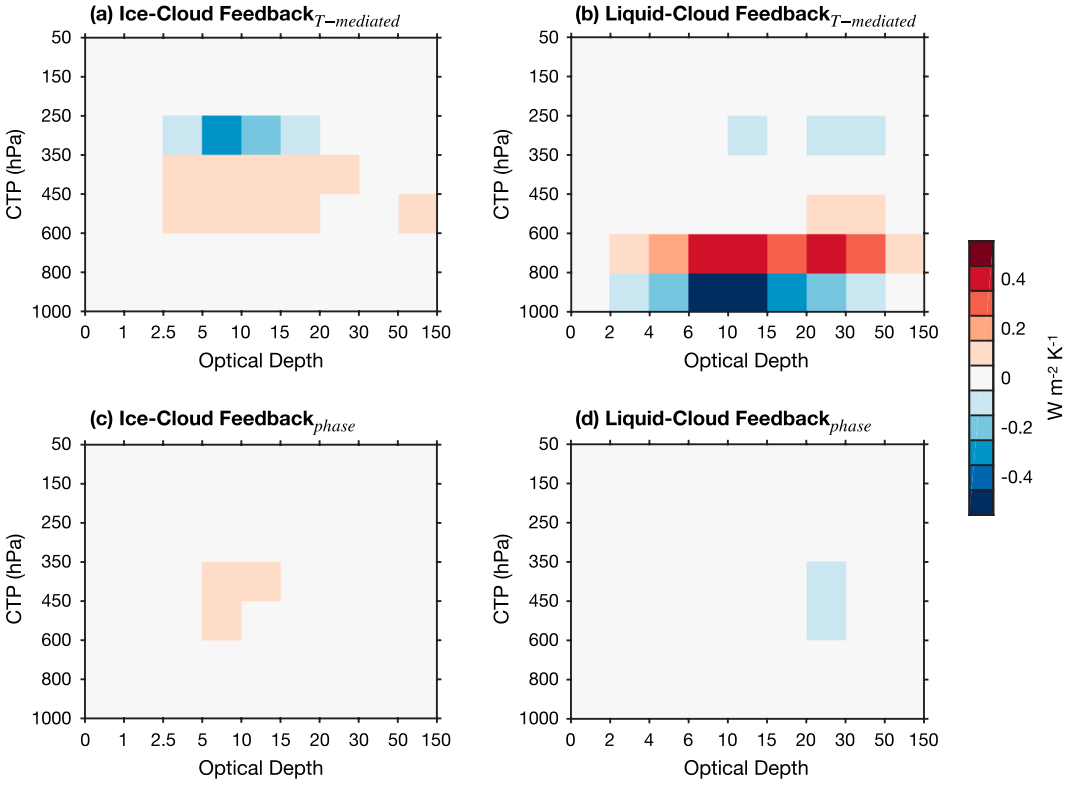

FIG. 3. Southern Ocean SW cloud feedback as a function of cloud-top pressure (CTP), optical depth, and phase: (a),(b) temperature-mediated feedback, and (c),(d) cloud-phase scattering feedback.

2002; Thompson et al. 2017; Jeevanjee and Fueglistaler 2020). Thus, as the atmosphere warms and isotherms rise, the highest ice clouds rise as well. A second dipole pattern shows that the top of low-level liquid clouds sinks as the atmosphere warms (Fig. 3b). This cloud response has been detected in other satellite and field observations, but the physical cause is not fully understood (Huang et al. 2016; Mace et al. 2021b). One possible explanation is that a warmer, more emissive free troposphere reduces cloud-top radiative cooling. This weakens turbulence and reduces the vertical development of boundary layer clouds (Eastman and Wood 2018).

In contrast to the temperature-mediated feedback, the cloud-phase scattering feedback has a strikingly different pattern (Figs. 3c,d). Throughout the troposphere the ice-cloud feedback is positive and the liquid-cloud feedback is negative, indicating an ice-to-liquid conversion. The feedback magnitude maximizes in the middle troposphere, where ice and liquid clouds both occur (Figs. 1a,b). It is not obvious from Fig. 3 how much the cloud-phase scattering feedback contributes to the total temperature-mediated feedback, but it is clear that other feedback mechanisms contribute as well.

The temperature-mediated and cloud-phase feedbacks can be compared more clearly by summing the components over the CTP dimension to remove dipole signals from vertical shifts in clouds. The prevailing signal of the temperature-mediated feedback for low-level clouds (CTP $>$ 600 hPa) is a dipole pattern along the optical depth dimension that shows an optical thinning of liquid cloud (Figs. 4a,b). Previous work suggests that this positive low-cloud optical depth feedback could be a consequence of reduced cloud-top radiative cooling, more frequent decoupling of clouds from the surface mixed layer, or more efficient drying from cloud-top entrainment (Terai et al. 2019; Mace et al. 2021b). Our results do not speak to the physical cause, but they do show that the cumulative effect of positive feedback mechanisms outweighs that of negative feedback mechanisms, including enhanced condensation in cloud updrafts and cloud-phase changes (Betts and Harshvardhan 1987; Lutsko and Cronin 2018). Indeed, the scattering component of cloud-phase feedback is negligible for low clouds because ice-topped clouds rarely occur at this level (Figs. 4d,e; see also Fig. 1).

The feedback from non-low clouds (CTP $\leq$ 600 hPa) has different characteristics. The temperature-mediated feedback includes an ice-to-liquid conversion, and the cloud-phase scattering feedback has the same sign but larger magnitude (Fig. 4). This difference in magnitude may be associated with non-low clouds shifting upward as the atmosphere warms (Fig. 3a). As clouds shift upward they experience less warming and therefore a reduced ice-to-liquid conversion compared to what would occur if they were to remain at fixed altitudes. The estimate of the cloud-phase scattering feedback represents phase conversions with fixed cloud altitudes, while the estimate of the temperature-mediated feedback includes the effect of upward shifts in clouds. Despite this difference,

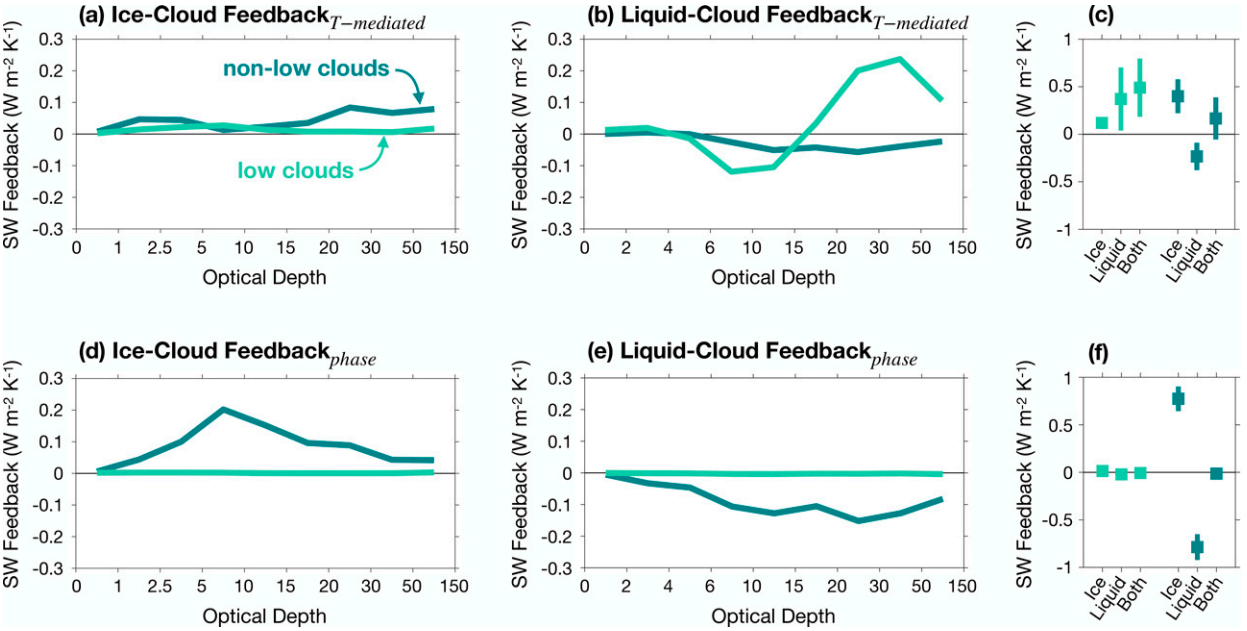

FIG. 4. SW feedbacks associated with low clouds and non–low clouds over the Southern Ocean. Low and non–low clouds are defined by CTP > 600 hPa and CTP ≤ 600 hPa, respectively. (a),(b) Ice- and liquid-cloud components of the temperature-mediated feedback as a function of optical depth. (c) Feedback components summed over the optical depth dimension. The sum of the liquid- and ice-cloud components is labeled "Both". Squares and lines show the mean and 95% confidence interval. (d)–(f) As in (a)–(c), but for the cloud-phase scattering feedback.

the results consistently show that the cloud-phase scattering feedback is primarily confined to free-tropospheric clouds.

We next sum the feedback components over the optical depth dimension to determine the total feedback. Low clouds exert a significant positive temperature-mediated feedback that mostly arises from liquid clouds, and non-low clouds exert counteracting ice and liquid feedbacks that sum to a near-zero value (Fig. 4c). The low-cloud component is largest, and thus the total feedback is positive (Fig. 5a). Low clouds dominate the mean cloud albedo over the Southern Ocean, so it is perhaps not surprising that they dominate the temperature-mediated feedback as well (Haynes et al. 2011; Bodas-Salcedo et al. 2016). In contrast, the cloud-phase scattering feedback is mostly limited to non-low clouds, and it consists of ice and liquid components that cancel very closely (Figs. 4f and 5a). The total temperature-mediated feedback summed over all CTP–optical depth–phase components is significantly positive (0.66 ± 0.32 W m^{-2} K^{-1}) and is an order of magnitude larger than the total cloud-phase scattering feedback (-0.02 ± 0.05 W m^{-2} K^{-1}). Thus, changes in cloud scattering properties arising from phase changes make a small contribution to the overall temperature-driven cloud feedback.

The smallness of the cloud-phase scattering feedback is surprising given that some modeling studies have reported much larger values (Ceppi et al. 2016a; Tan et al. 2016; Frey and Kay 2018). To interpret this result, we decompose the feedback into contributions from changes in 1) optical depth τ; 2) single-scattering albedo $\tilde{\omega}$, which represents the relative importance of scattering and absorption; and 3) the asymmetry parameter g, which embodies the scattering angles of cloud particles. The decomposition reveals that phase changes cause a negative optical depth feedback (Fig. 5b). This is consistent with the expectation that ice-to-liquid conversions result in smaller but more numerous cloud particles, which increases the particle surface-area-to-volume ratio and hence the bulk optical depth. The decomposition also reveals an offsetting positive feedback from changes in the asymmetry parameter and single-scattering albedo. Ice and liquid particles absorb about the same fraction of incident broadband SW radiation (Petty 2006), so this feedback component is dominated by changes in scattering angles. For instance, in our main radiative kernels, the asymmetry parameter for visible radiation is about 0.80 for ice clouds and 0.87 for liquid clouds (Fu 1996; Hu and Stamnes 1993). Thus, when cloud particles scatter visible radiation in single scattering events, ice particles typically scatter about 90% of the radiant energy in the forward hemisphere, while liquid droplets scatter about 93% of the energy forward (Sagan and Pollack 1967). Converting ice to liquid therefore enhances forward scattering, which reduces cloud albedo. The magnitude of this feedback component may be somewhat sensitive to the microscopic properties of cloud particles that are assumed when calculating the kernels, but the confidence intervals account for much of this uncertainty by incorporating particle-size uncertainty and using two ice optical property schemes (appendix B). Furthermore, the radiative transfer model assumes that ice particles have a smooth surface (Fu 1996; Ebert and Curry 1992). Incorporating surface roughness would enhance backscattering by ice particles and thereby increase the component of cloud-phase feedback that is associated with changes in scattering angles (Fu 2007). The main interpretation is therefore robust: Converting ice to liquid increases cloud optical depth and shifts the scattering angles of cloud particles toward the forward

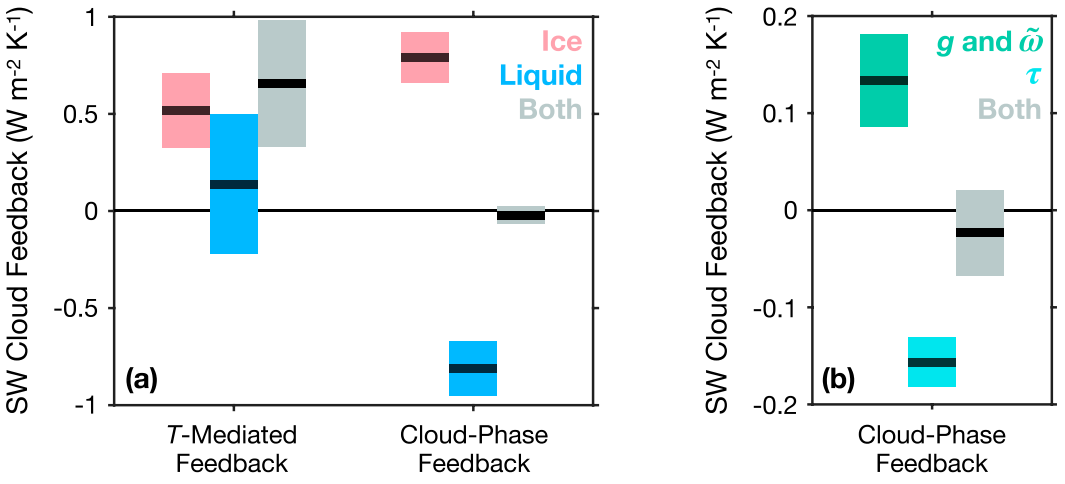

FIG. 5. Mean SW cloud feedback over the Southern Ocean. (a) Temperature-mediated feedback and cloud-phase scattering feedback for ice clouds, liquid clouds, and both phases combined. Lines and colored bars show the mean and 95% confidence interval. (b) Cloud-phase scattering feedback decomposed into contributions from changes in cloud-particle asymmetry parameter and single-scattering albedo (g and $\tilde{\omega}$) and cloud optical depth (τ).

direction. These counteracting feedback components make the overall cloud-phase scattering feedback small.

All of these feedback values are inferred from observed natural variability, so they are contingent on the assumptions of the methodology and the limitations of the observations. However, we tested the sensitivity of the results to the most salient of these assumptions and limitations. For instance, the feedback analysis treats clouds as either entirely liquid or entirely ice (Zelinka et al. 2012) based on MODIS cloud-phase observations, which retrieve phase only at cloud top. Sensitivity to this retrieval limitation is tested by matching MODIS pixels with coincident radar/lidar measurements that identify phase below cloud top. The combination of sensors is used to distinguish ice, pure liquid, and liquid-topped mixed-phase clouds, and the cloud-phase scattering feedback is estimated while allowing for transitions between the three phase categories. We also checked sensitivity to satellite retrieval bias from large solar zenith angle and multilayer clouds, and we checked sensitivity to observing platform and time period. The envelope of feedback uncertainty from the sensitivity tests is close to that of the main estimates (appendix C). Thus, these assumptions and limitations do not affect the main results.

4. Implications for climate sensitivity

We next frame the results in the context of the existing literature to show their implications for climate sensitivity. A recent survey by Sherwood et al. (2020) identified high-latitude (40°–70°) low-cloud optical depth feedback as one of six primary components of global cloud feedback. Observational studies have argued that this feedback component could be positive (Tselioudis et al. 1992; Norris and Iacobellis 2005; Huang et al. 2016; Terai et al. 2016; Tan et al. 2019; Mace et al. 2021b; Myers et al. 2021) or negative (McCoy et al. 2014b; Ceppi et al. 2016b). Sherwood et al. (2020) therefore established a consensus estimate with a central value of zero and a confidence interval wide enough to include positive and negative feedback values estimated by Terai et al. (2016) and Ceppi et al. (2016b). The consensus feedback was then combined with other evidence to estimate the overall cloud feedback and the equilibrium response of global-mean surface temperature to doubling atmospheric CO_2. The temperature response was represented by effective climate sensitivity (Gregory et al. 2004).

Our findings support a different interpretation of high-latitude low-cloud optical depth feedback. First, we find that the feedback is positive over the Southern Ocean. We estimate that the mean temperature-mediated low-cloud optical depth feedback is 0.55 ± 0.28 W m^{-2} K^{-1} over ice-free ocean between 40° and 60°S. Extending the domain to 40°–70°S to match the analysis of Sherwood et al. (2020) results in a similar feedback of 0.55 ± 0.26 W m^{-2} K^{-1}, although we note that the area of ice-free ocean is much smaller between 60° and 70°S than in the rest of the domain. Second, we find that the negative feedback estimate on which the consensus value is based is probably biased because it does not control for the confounding influence of wind and boundary layer inversion strength when estimating the temperature-mediated cloud feedback (appendix C; Ceppi et al. 2016b). Third, our results show that it is very unlikely that phase conversions in low clouds will produce a substantial negative optical depth feedback over the Southern Ocean (Fig. 4). Collectively these findings indicate that high-latitude low-cloud optical depth feedback is likely positive.

We investigate the global implications of these results using the framework of Sherwood et al. (2020). Following their analysis, we begin with our estimate of low-cloud optical depth feedback over ice-free ocean between 40° and 70°S. We then assume that the high-latitude low-cloud optical depth feedback in the Southern Hemisphere is dominated by regions of ice-free ocean and is 3.8 times larger than the corresponding feedback in the Northern Hemisphere (M. D. Zelinka 2021, personal communication). These assumptions are based on the analysis of Terai et al. (2016). We then scale the estimate

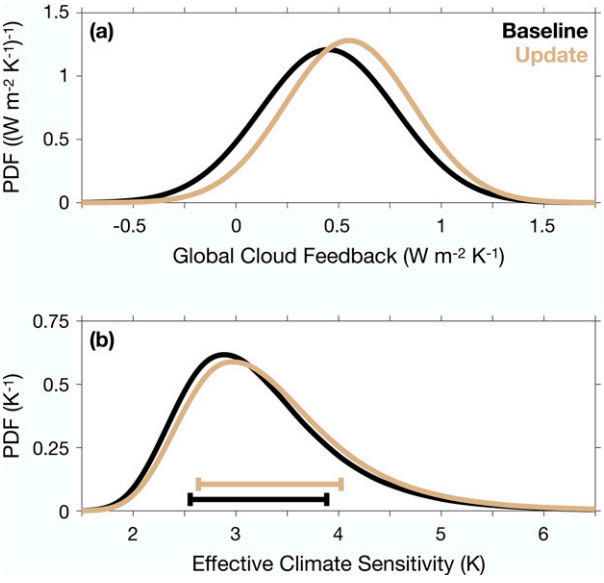

FIG. 6. Implications of the feedback constraints for climate sensitivity. The "Baseline" case shows results from the analysis of Sherwood et al. (2020), and the "Update" case is similar except that it uses our estimate of high-latitude low-cloud optical depth feedback. Probability density functions (PDFs) are shown for (a) global cloud feedback and (b) effective climate sensitivity. Horizontal lines in (b) show the 66% confidence range.

of high-latitude low-cloud optical depth feedback by the fraction of global surface area that is between 40° and 70° latitude to determine the contribution to global cloud feedback. This yields a global feedback of 0.10 ± 0.02 W m^{-2} K^{-1} (one standard deviation). Our feedback estimate has a more positive central value and a narrower confidence interval than the value of 0.0 ± 0.1 W m^{-2} K^{-1} (one standard deviation) assessed by Sherwood et al. (2020). Finally, we estimate effective climate sensitivity by performing the "Baseline" calculation of Sherwood et al. (2020) with our feedback estimate in place of their assessed value. Our feedback constraint slightly narrows the probability distribution of the overall global cloud feedback, and it increases the modal value from 0.45 to 0.55 W m^{-2} K^{-1} (Fig. 6a). Consequently, the 66% confidence range for climate sensitivity increases from 2.55–3.88 to 2.63–4.02 K (Fig. 6b). Our observational constraint thus shifts the bounds of the "likely" range of climate sensitivity by about +0.1 K.

5. Conclusions

Southern Ocean clouds have large radiative effects that shape global climate (Hwang and Frierson 2013; Kay et al. 2016; Hawcroft et al. 2017). They are also especially difficult to simulate, so observations offer a valuable alternative path toward understanding their radiative feedbacks (Trenberth and Fasullo 2010). Here we use MODIS observations to infer Southern Ocean SW cloud feedback as a function of cloud-top phase. The temperature-mediated feedback includes contributions from an optical thinning of low clouds and an ice-to-liquid conversion in free-tropospheric clouds (Figs. 3 and 4). The low-cloud feedback dominates, causing the overall temperature-mediated feedback to be positive (Fig. 5). These constraints imply a higher climate sensitivity than a recent consensus estimate of cloud feedback (Fig. 6).

In addition to constraining SW cloud feedback, another key goal is to decompose the feedback into contributions from particular physical mechanisms. Such a decomposition is essential for understanding the climate response to external forcing. Here we leverage the new feedback methodology to isolate one mechanism: the cloud-phase scattering feedback. This mechanism increases cloud optical depth and shifts the scattering angles of cloud particles toward the forward direction. The resulting feedback components offset one another, and thus the cloud-phase scattering feedback is an order of magnitude smaller than the overall temperature-mediated feedback (Fig. 5). These results do not preclude the possibility that changes in cloud phase will cause a substantial cloud-amount feedback by changing precipitation efficiency (Mülmenstädt et al. 2021), nor do they reveal which mechanisms dominate the temperature-mediated feedback. However, the results do reveal a robust constraint on Southern Ocean cloud feedback: Although the dominant feedback mechanisms remain elusive, it is very unlikely that the cloud-phase scattering feedback is one of them.

Acknowledgments. We thank Tim Carlsen, Nick Lutsko, Peter Blossey, and Qiang Fu for helpful discussions and Jay Mace and two anonymous reviewers for their comments. C.J.W. was supported by the NOAA Climate and Global Change Postdoctoral Fellowship Program, administered by UCAR's Cooperative Programs for the Advancement of Earth System Science (CPAESS) under Award NA18NWS4620043B. C.J.W. and J.R.N. were also supported by NASA under Grant 80NSSC18K1020.

Data availability statement. The datasets used in this study include 1) MODIS Collection 6 versions MYD08_M3 and MOD08_M3, 2) ERA5, 3) Clouds and the Earth's Radiant Energy System (CERES) Energy Balanced and Filled Edition 4.1, 4) *CloudSat* data products 2B-CLDCLASS-LIDAR and MOD06-1KM-AUX version P1_R05, and 5) CMIP6 model output. These data are publicly available at https://earthdata.nasa.gov/, https://cds.climate.copernicus.eu/cdsapp#!/dataset/reanalysis-era5-pressure-levels-monthly-means?tab=overview, https://ceres.larc.nasa.gov/data/, http://www.cloudsat.cira.colostate.edu/, and https://esgf-node.llnl.gov/projects/cmip6/, respectively. The radiative transfer model used in this study is available at http://rtweb.aer.com/rrtm_frame.html, and the code for the climate-sensitivity analysis is available at https://doi.org/10.5281/zenodo.3945276. The feedback estimates are listed in Table S3 in the online supplemental material for reproducibility.

APPENDIX A

Validation of Radiative Kernels

SW cloud radiative effect (CRE) is defined as the difference between all-sky and clear-sky SW flux at the top of

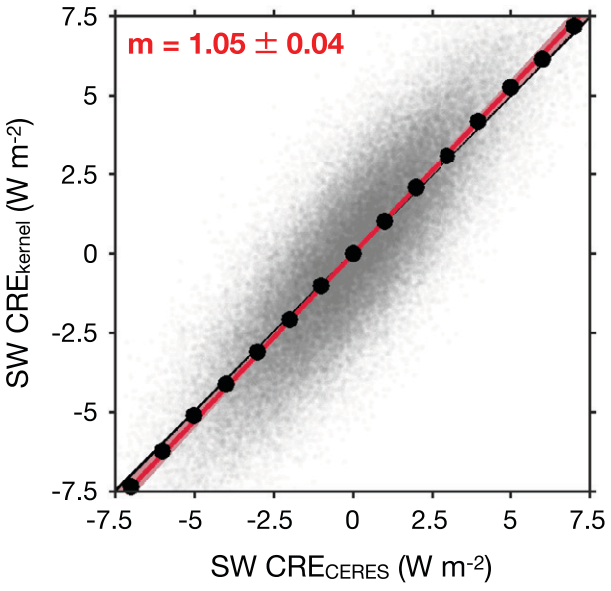

FIG. A1. Validation of the radiative kernels. Kernel-predicted SW cloud radiative effect (SW CRE_{kernel}) is plotted as function of observed SW cloud radiative effect (SW CRE_{CERES}). Gray dots are individual data points, and black dots are conditional means of SW CRE_{kernel} as a function of SW CRE_{CERES}. The red line and shading show the regression line and its 95% confidence interval. The regression slope is in the top-left corner.

the atmosphere. We validate the radiative kernels by using them to predict monthly anomalies of SW CRE:

$$\text{SW CRE}_{\text{kernel}} = \sum_i c_i K_i, \tag{3}$$

where i runs over all MODIS histogram bins, c_i is the monthly cloud-fraction anomaly reported by MODIS, and K_i is the kernel. SW CRE_{kernel} is compared with observed values from Clouds and the Earth's Radiant Energy System (CERES) satellite data (SW CRE_{CERES}; Loeb et al. 2018). Monthly SW CRE anomalies are averaged over 1-yr intervals for consistency with the annual-mean SW cloud-feedback estimates, and SW CRE_{kernel} is regressed on SW CRE_{CERES} using all data from the study domain. The regression agrees very well with conditional means of SW CRE_{kernel} as a function of SW CRE_{CERES}, indicating that linear regression accurately represents the bias of the kernel method (Fig. A1). If m is the regression slope, then $m - 1$ is the bias of the magnitude of SW CRE_{kernel}. We find that $m = 1.05 \pm 0.04$ (95% confidence interval). This indicates that the kernels will overestimate the magnitude of SW cloud feedback by 5% ± 4%.

APPENDIX B

Uncertainty

Cloud feedback is inferred from observed cloud–temperature relationships, radiative kernels, and model projections of CO_2-forced warming, so all three terms contribute to feedback uncertainty. These uncertainty components are independent, so they are calculated separately and then combined. We illustrate the uncertainty analysis by describing the calculation of the 95% confidence interval for the mean temperature-mediated feedback for both cloud phases combined.

The first source of feedback uncertainty arises from uncertainty in cloud–temperature regression slopes. Let γ represent the standard error of the feedback summed over all MODIS histogram bins for a given latitude and calendar month. We estimate γ as

$$\gamma = \sqrt{\sum_i \sum_j \left(\sigma_i K_i \frac{dT_i}{dT_{2\text{m}}}\right)\left(\sigma_j K_j \frac{dT_j}{dT_{2\text{m}}}\right) r_{i,j}},$$

where i and j run over all histogram bins; σ_i is the standard error of regression slope $\partial c_i/\partial T_i$; $r_{i,j}$ is the correlation between cloud-fraction anomalies in bins i and j; and central estimates are used for K_i, K_j, $dT_i/dT_{2\text{m}}$, and $dT_j/dT_{2\text{m}}$. Central estimates for the K terms are calculated following the method described in section 2b, and central estimates for the $dT/dT_{2\text{m}}$ terms are determined by the CMIP6 multimodel mean. The γ terms are then combined to account for averaging over the seasonal cycle:

$$\delta = \frac{1}{12}\sqrt{\sum_n \gamma_n^2},$$

where n runs over all calendar months. The δ terms are combined further to account for averaging over latitude:

$$\boldsymbol{\delta} = \sqrt{\sum_l \delta_l^2 w_l^2} \Big/ \sum_l w_l,$$

where l runs over all latitude bins and w_l is a weighting factor that is proportional to the area of ice-free ocean in bin l. Finally, the confidence interval is scaled to account for the number of effective degrees of freedom. Serial correlation is diagnosed from SW CRE as defined by Eq. (3). The ratio of nominal to effective spatial degrees of freedom, N_s/N_s^*, is estimated using Eq. (5) of Bretherton et al. (1999), and the ratio of nominal to effective temporal degrees of freedom is estimated by

$$N_t/N_t^* = \frac{1+r}{1-r},$$

where r is the lag-1 autocorrelation of SW CRE. Values of N_t/N_t^* are calculated for every spatial grid point and then averaged. The half width of the 95% confidence interval for the mean feedback due to regression-slope uncertainty is

$$\Delta_1 = \beta\boldsymbol{\delta}\sqrt{\frac{N_s}{N_s^*}\frac{N_t}{N_t^*}},$$

where β is the critical value of a Student's t distribution at the $(1 - \alpha/2)100\%$ significance level using $N_s^* N_t^* - 6$ degrees of freedom and $\alpha = 0.05$.

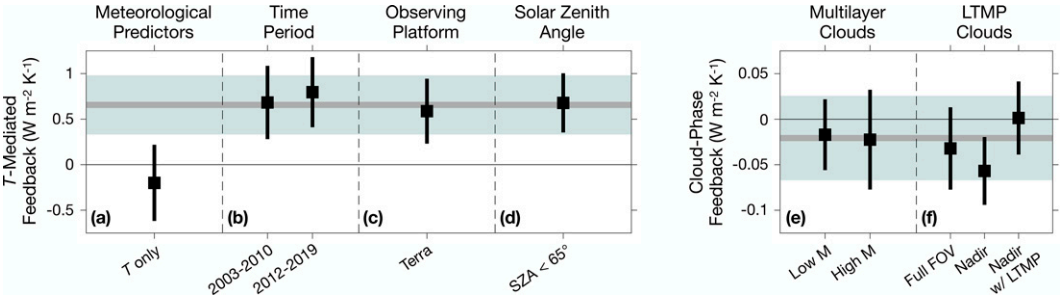

FIG. C1. Summary of sensitivity tests, showing the (a)–(d) temperature-mediated cloud feedback and (e),(f) cloud-phase scattering feedback. The plotted values represent feedbacks from all cloud phases combined. Gray lines and shading show the mean and 95% confidence interval for the main estimates, and black squares and lines show the mean and 95% confidence interval for the sensitivity tests. (a) Sensitivity to whether or not wind and boundary layer inversion strength are controlled for in the regression model. The "T only" case estimates the feedback using only temperature as a predictor. (b) Sensitivity to time period. The "2003–10" and "2012–19" cases estimate feedbacks using the earliest and latest 8-yr periods of the record. (c) Sensitivity to observing platform. The "Terra" case estimates the feedback using MODIS data from the *Terra* satellite. (d) Sensitivity to bias from large solar zenith angle (SZA). The "SZA $< 65°$" case estimates the feedback using MODIS data that are not affected by bias from large SZA. (e) Sensitivity to multilayer clouds. The "Low M" and "High M" cases estimate feedbacks using subsets that have relatively low and high proportions of data with suspected multilayer-cloud bias. (f) Sensitivity to the treatment of liquid-topped mixed-phase clouds (LTMP). The "Full FOV" case estimates the feedback using the full MODIS dataset and applying the compositing technique that is introduced to accommodate radar/lidar data (see text). The "Nadir" case is similar but uses the near-nadir subset of MODIS pixels that are collocated with radar/lidar measurements. The "Nadir w/LTMP" case is similar to the "Nadir" case except that the feedback is estimated with transitions between three phase categories: ice, pure liquid, and LTMP.

The second source of uncertainty arises from assumptions about cloud microphysical properties that are made when calculating the radiative kernels. We assume a mean and 95% confidence interval for cloud-droplet effective radius of 14 ± 3 μm, which spans the range of values throughout the climatological seasonal cycle from three MODIS-derived products (McCoy et al. 2014a). We also assume a mean and 95% confidence interval for ice-crystal effective radius of 35 ± 10 μm based on satellite radar/lidar observations (McCoy et al. 2014a). Finally, we use two ice optical property schemes that are based on different observed particle-size distributions (Fu 1996; Ebert and Curry 1992). Radiative kernels are calculated with the upper and lower bounds of particle size and with both ice optical property schemes, and feedbacks are calculated using the modified kernels. Central estimates of $\partial c_i/\partial T_i$ and dT_i/dT_{2m} are used in the calculations. The component of feedback uncertainty that is associated with particle-size uncertainty is defined such that the confidence interval just encompasses the feedback values of both the upper and lower bounds of particle size. Variations in feedback values from the kernel modifications are added in quadrature to determine their cumulative contribution to cloud-feedback uncertainty Δ_2.

The final source of uncertainty arises from the spread in model projections of CO_2-forced warming. We estimate this uncertainty component by calculating feedbacks using dT_i/dT_{2m} values from each of the 34 CMIP6 models. Central estimates of $\partial c_i/\partial T_i$ and K_i are used in the calculations. The 95% confidence interval Δ_3 is defined such that the interval just encompasses the second-largest and second-smallest feedback values.

After computing the three uncertainty terms, the half width of the 95% confidence interval for the mean temperature-mediated feedback Δ_{net} is calculated by adding the terms in quadrature:

$$\Delta_{net} = \sqrt{\Delta_1^2 + \Delta_2^2 + \Delta_3^2}.$$

Confidence intervals for other feedback components are calculated similarly.

APPENDIX C

Bias

Here we investigate sensitivity of the results to several assumptions of the methodology and limitations of the observations. We consider the meteorological predictors used in the regression model, the time period of analysis, and the observing platform. We also investigate satellite retrieval bias from large solar zenith angle, multilayer clouds, liquid-topped mixed-phase clouds, and partly cloudy pixels. The sensitivity tests are described below and summarized in Fig. C1.

a. Meteorological predictors

Three studies including ours have reported estimates and confidence intervals for Southern Ocean SW cloud feedback inferred from MODIS data. Terai et al. (2016, hereafter T16) estimated that the mean SW low-cloud optical depth feedback between 40° and 70°S is 0.38 ± 0.25 W m^{-2} K^{-1}; Ceppi et al. (2016b, hereafter C16) estimated that the mean temperature-mediated feedback between 45° and 60°S is

-0.76 ± 0.82 W m^{-2} K^{-1} relative to local warming between 500 and 850 hPa; and we estimate that the mean temperature-mediated feedback over ice-free ocean between 40° and 60°S is 0.66 ± 0.32 W m^{-2} K^{-1}. Our results are consistent with the estimate of T16 and inconsistent with the estimate of C16. Here we attempt to reconcile this discrepancy.

One difference among the three studies is that each one treats confounding meteorological factors differently in their regression models. Our study controls for the monthly three-dimensional wind field and estimated inversion strength. T16 include changes in inversion strength in their feedback estimate, and they filter the data for low clouds, which controls for most of the confounding influence of large-scale vertical motion. C16 regress cloud properties on temperature anomalies without controlling for other meteorological factors. To check if this matters, we align our analysis with that of C16 by estimating feedbacks using only temperature as a predictor in the regression model. The temperature-only model predicts a temperature-mediated SW cloud feedback that is significantly more negative (Fig. C1a). Furthermore, we also check the results by applying the method of C16 to our cloud histograms and kernels. This yields a mean temperature-mediated feedback estimate of -0.48 ± 0.82 W m^{-2} K^{-1} between 45° and 60°S relative to local warming between 500 and 850 hPa, which is consistent with the value of -0.76 ± 0.82 W m^{-2} K^{-1} reported by C16. These results show that the treatment of confounding meteorological factors is probably the main reason for the discrepancy among the studies.

The relative importance of confounding meteorological factors can be estimated based on their correlation with temperature (Scott et al. 2020). For a given MODIS histogram bin i, a confounding meteorological variable x_i will bias the estimate of the temperature-mediated cloud feedback from the temperature-only regression model by an amount F_{SW,x_i} given by

$$F_{\mathrm{SW},x_i} = \frac{\partial c_i}{\partial x_i}\frac{dx_i}{dT_i}K_i\frac{dT_i}{dT_{2\mathrm{m}}}.$$

Based on this equation, we find that estimated inversion strength and meridional wind are the two most important confounding factors that affect the temperature-only regression model over the Southern Ocean. This relationship exists because warm atmospheric temperature anomalies tend to occur with anomalous poleward wind and enhanced inversion strength in the context of natural variability (Wall et al. 2017). Failure to control for wind and inversion strength in the regression model will therefore significantly bias the estimate of the temperature-mediated cloud feedback and potentially introduce a sign error.

b. Time period

Our analysis assumes that extratropical cloud–temperature relationships will not substantially change as the climate responds to anthropogenic radiative forcing. This assumption has been verified in many model projections of anthropogenic climate change (Gordon and Klein 2014; Terai et al. 2016; Ceppi et al. 2016b), although it does not hold in every model (Bjordal et al. 2020). To check the assumption further, we compare temperature-mediated feedbacks inferred from the first eight years (2003–10) and the final eight years (2012–19) of the 17-yr MODIS record. The feedbacks inferred from the two periods are similar to one another and to the main estimate (Fig. C1b). This provides some additional support for the assumption of time-invariant cloud–temperature relationships, at least for decadal climate changes.

c. Observing platform

Our main analysis infers feedbacks using MODIS data from the *Aqua* satellite. We also check the results using MODIS data from the *Terra* satellite because MODIS-*Terra* is calibrated differently and acquires data in the morning rather than the afternoon. The temperature-mediated feedbacks inferred from MODIS-*Aqua* and MODIS-*Terra* are similar, so the results are not sensitive to the observing platform (Fig. C1c).

d. Solar zenith angle

In addition to temporal sampling limitations, MODIS data have systematic biases that occur during certain conditions. The first bias we consider is associated with solar zenith angle (SZA). The MODIS cloud retrieval algorithms assume that radiative transfer in each pixel is plane parallel and is independent of the properties of the surrounding area. These assumptions break down when SZA $> 65°$, which biases the cloud data (Grosvenor and Wood 2014). We investigate the implications of this bias by screening the data based on SZA. Latitude–month combinations are considered to have "good" data if SZA $< 65°$ at the data acquisition time for all pixel-level measurements, and latitude–month combinations are considered to have "varied" data otherwise. Sensitivity to SZA bias is checked by calculating the temperature-mediated feedback using only "good" data. Regression slopes from latitude–month combinations with "varied" data are replaced with regression slopes from the same latitude and the closest calendar month with "good" data. When two months are equally close, then their regression slopes are averaged. After applying these substitutions, the resulting feedback estimate is similar to the main estimate, indicating that SZA bias does not influence the results (Fig. C1d). This is probably because the bias does not affect data during spring and summer, when insolation is largest.

e. Multilayer clouds

Other MODIS biases are especially relevant to the cloud-phase scattering feedback. For instance, the presence of multilayer clouds can cause errors in the retrievals of CTP and cloud-top phase. We investigate this bias using the MODIS multilayer-cloud quality assurance flag, which identifies pixels that are suspected to be adversely affected by multilayer clouds. The proportion of cloudy scenes affected by multilayer clouds is

$$M = N_{\mathrm{ML}}/N_{\mathrm{cloud}},$$

where N_{ML} is the number of pixels with potentially problematic multilayer clouds and N_{cloud} is the total number of

cloudy pixels. For each latitude–calendar month combination, high-M and low-M composites are created from data with above-median and below-median values of M, respectively. The cloud-phase scattering feedback is then estimated separately for the two composites. The M difference between the high and low composites is 2.4 times smaller than the mean value of M for the whole dataset, so the high-M-minus-low-M feedback difference is scaled by a factor of 2.4 to estimate the feedback bias from multilayer clouds. Even after applying the scaling factor, the high-M-minus-low-M difference is very small (Fig. C1e). Thus, multilayer clouds do not bias the estimate of the cloud-phase scattering feedback.

f. Liquid-topped mixed-phase clouds

Another data limitation that is relevant to cloud-phase feedback is the fact that MODIS retrieves phase only at cloud top. Field observations indicate that liquid-topped clouds over the Southern Ocean can be either pure-liquid clouds or mixed-phase clouds with supercooled liquid at cloud top and ice below (Mace et al. 2021a,b). Because MODIS cloud-phase data are limited to cloud top, MODIS cannot distinguish liquid-topped mixed-phase (LTMP) clouds from pure-liquid clouds, so our main analysis treats these clouds as a single phase category. Consequently, if LTMP clouds convert to pure-liquid clouds as they warm, then the associated feedback component would not be included in our estimate of cloud-phase scattering feedback. We therefore need to estimate this component using another method.

LTMP clouds are investigated using MODIS data and radar/lidar data from the *CloudSat* and *CALIPSO* satellites. Footprint data are analyzed from the *CloudSat* MOD06-1KM-AUX and 2B-CLDCLASS-lidar datasets from June 2006 through April 2011 (Sassen et al. 2008; Zhang et al. 2010). The radar/lidar data detect phase below cloud top and label cloud layers as liquid, ice, or mixed phase. Each radar/lidar profile is matched with the collocated MODIS pixel and the adjacent pixel on either side in the across-track direction. MODIS pixels are then gridded by latitude, longitude, and month, and cloud-fraction histograms are compiled as a function of CTP, optical depth, and phase.

Although the radar/lidar data provide valuable additional information, they also have sampling limitations that motivate minor changes to the methodology. Specifically, the radar and lidar are nadir-staring instruments, so all of the collocated MODIS pixels are viewed at nadir. These data differ from the full MODIS dataset because of viewing angle dependencies (Maddux et al. 2010). Furthermore, nadir sampling causes the number of MODIS pixels to vary by several orders of magnitude between grid boxes, which is problematic for applying linear regression. We accommodate this issue by calculating $\partial P_{\mathrm{liq}}/\partial T$ by compositing. For each CTP–latitude–calendar month combination, warm and cold composites are created from the data with above-median and below-median temperature anomalies. The value of $\partial P_{\mathrm{liq}}/\partial T$ is then calculated from the warm-minus-cold composite difference of the mean values of P_{liq} and T weighted by the number of cloudy pixels in each grid box. Sampling uncertainty is then estimated by bootstrapping. Data are separated into blocks with dimensions of 10° latitude, 10° longitude, and 1 month so that each block has approximately one degree of freedom. Data blocks are randomly selected with replacement to create 1000 bootstrap samples of the observations, and cloud-phase scattering feedback is estimated from each sample. The 95% confidence interval associated with sampling uncertainty (Δ_1) is then determined by the interval that just encompasses the 2.5th and 97.5th percentiles of the feedback values from the bootstrapping calculation. All other aspects of the cloud-phase feedback methodology are carried out as before.

Figure C1f shows cloud-phase scattering feedback estimated by this method. The first two cases show the effects of the methodological and viewing geometry differences one at a time. The "Full FOV" case is the feedback estimated using the full MODIS dataset and calculating $\partial P_{\mathrm{liq}}/\partial T$ by compositing, and the "Nadir" case is similar except that it uses near-nadir MODIS data that are collocated with radar/lidar measurements. Feedback estimates from these cases are consistent with one another and with the main estimate. Thus, the differences in methodology and viewing geometry do not significantly affect the results.

Having established the feedback of the "Nadir" case, we now leverage the radar/lidar data to distinguish pure-liquid clouds from LTMP clouds. MODIS pixels that coincide with radar/lidar data are assigned to one of three phase categories: 1) "ice" when MODIS reports ice, 2) "pure liquid" when MODIS reports liquid and radar/lidar reports that the highest liquid-containing cloud is pure liquid, and 3) "LTMP" when MODIS reports liquid and radar/lidar reports that the highest liquid-containing cloud is mixed phase or that all clouds are ice. The climatology of the cloud-fraction histograms for the three phase categories is shown in Fig. C2. As expected from previous work, pure-liquid clouds occur most often in the boundary layer, and LTMP clouds occur between the surface and the middle troposphere (Zhang et al. 2010). The presence of pure-liquid cloud in the boundary layer is also consistent with field observations that sample cloud profiles more completely near the surface (Mace et al. 2021b).

The ability to distinguish pure-liquid and LTMP clouds facilitates a revised estimate of cloud-phase scattering feedback with three phase categories. For a given CTP bin, the proportion of total cloud fraction in each phase is

$$P_{\mathrm{ice}} = \frac{C_{\mathrm{ice}}}{C_{\mathrm{ice}} + C_{\mathrm{pl}} + C_{\mathrm{LTMP}}},$$

$$P_{\mathrm{pl}} = \frac{C_{\mathrm{pl}}}{C_{\mathrm{ice}} + C_{\mathrm{pl}} + C_{\mathrm{LTMP}}},$$

$$P_{\mathrm{LTMP}} = \frac{C_{\mathrm{LTMP}}}{C_{\mathrm{ice}} + C_{\mathrm{pl}} + C_{\mathrm{LTMP}}},$$

where the subscripts ice, pl, and LTMP represent ice, pure liquid, and LTMP phases, respectively. We calculate $\partial C_{\mathrm{ice}}/\partial T$,

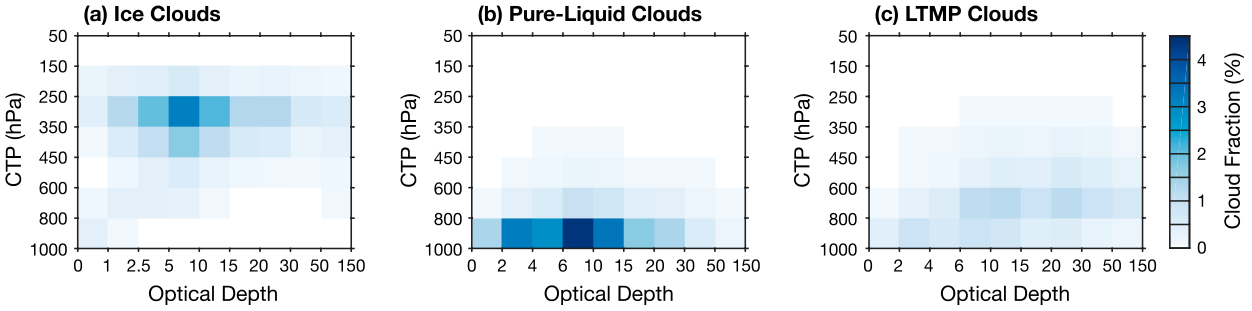

FIG. C2. Climatology of cloud fraction over the Southern Ocean from MODIS data that are collocated with radar/lidar measurements from the *CloudSat* and *CALIPSO* satellites: (a) ice, (b) pure-liquid, and (c) liquid-topped mixed-phase (LTMP) clouds.

$\partial C_{\mathrm{pl}}/\partial T$, and $\partial C_{\mathrm{LTMP}}/\partial T$ and partition the values among the optical depth bins similarly to the main methodology. Finally, liquid condensate in LTMP clouds is assumed to be radiatively dominant over ice (Shupe et al. 2008), so the liquid-cloud kernel is used to calculate feedbacks for LTMP clouds. This method accounts for feedbacks that arise from transitions between any of the three phase categories, so it includes the component from LTMP-to-pure-liquid transitions that is missing from the main analysis.

The resulting feedback estimate is shown by the "Nadir w/LTMP" case in Fig. C1f. This estimate is consistent with the first two cases and with the main estimate. Thus, the fact the MODIS is unable to distinguish LTMP and pure-liquid clouds does not affect the main conclusions. This lack of sensitivity occurs because we calculate the cloud-phase scattering feedback separately for each CTP interval. LTMP and pure-liquid clouds mostly coexist in the two CTP intervals that are closest to the surface, and LTMP and pure-liquid clouds have similar optical depth distributions in these intervals (Fig. C2).

g. Partly cloudy pixels

The final data limitation we consider is the fact that MODIS excludes partly cloudy pixels when compiling monthly histograms. This could introduce a sampling bias if cloud elements that entirely cover pixels respond to warming differently than cloud elements that partially cover pixels. Fully and partly cloudy pixels make up 70.2% and 5.9% of the observations, respectively, and the partly cloudy cases include 5.7% liquid clouds and 0.2% ice clouds. The partly cloudy pixels are probably mostly associated with the edges of liquid clouds in the boundary layer, where the estimated cloud-phase scattering feedback is small. Thus, it is unlikely that excluding partly cloudy pixels affects the estimate of cloud-phase scattering feedback.

REFERENCES

Armour, K., J. Marshall, J. Scott, A. Donohoe, and E. R. Newsom, 2016: Southern Ocean warming delayed by circumpolar upwelling and equatorward transport. *Nat. Geosci.*, **9**, 549–554, https://doi.org/10.1038/ngeo2731.

Betts, A. K., and Harshvardhan, 1987: Thermodynamic constraint on the cloud liquid water feedback in climate models. *J. Geophys. Res.*, **92**, 8483–8485, https://doi.org/10.1029/JD092iD07p08483.

Bjordal, J., T. Storelvmo, K. Alterskjær, and T. Carlsen, 2020: Equilibrium climate sensitivity above 5°C plausible due to state-dependent cloud feedback. *Nat. Geosci.*, **13**, 718–721, https://doi.org/10.1038/s41561-020-00649-1.

Bodas-Salcedo, A., P. G. Hill, K. Furtado, K. D. Williams, P. R. Field, J. C. Manners, P. Hyder, and S. Kato, 2016: Large contribution of supercooled liquid clouds to the solar radiation budget of the Southern Ocean. *J. Climate*, **29**, 4213–4228, https://doi.org/10.1175/JCLI-D-15-0564.1.

Bretherton, C. S., M. Widmann, V. P. Dymnikov, J. M. Wallace, and I. Bladé, 1999: The effective number of spatial degrees of freedom of a time-varying field. *J. Climate*, **12**, 1990–2009, https://doi.org/10.1175/1520-0442(1999)012<1990:TENOSD>2.0.CO;2.

Ceppi, P., and D. L. Hartmann, 2015: Connections between clouds, radiation, and midlatitude dynamics: A review. *Curr. Climate Change Rep.*, **1**, 94–102, https://doi.org/10.1007/s40641-015-0010-x.

——, ——, and M. J. Webb, 2016a: Mechanisms of the negative shortwave cloud feedback in middle to high latitudes. *J. Climate*, **29**, 139–157, https://doi.org/10.1175/JCLI-D-15-0327.1.

——, D. T. McCoy, and D. L. Hartmann, 2016b: Observational evidence for a negative shortwave cloud feedback in middle to high latitudes. *Geophys. Res. Lett.*, **43**, 1331–1339, https://doi.org/10.1002/2015GL067499.

Clough, S. A., E. J. Mlawer, J. S. Delamere, M. J. Iacono, K. Cady-Pereira, S. Boukabara, and P. D. Brown, 2005: Atmospheric radiative transfer modeling: A summary of the AER codes. *J. Quant. Spectrosc. Radiat. Transfer*, **91**, 233–244, https://doi.org/10.1016/j.jqsrt.2004.05.058.

Eastman, R., and R. Wood, 2018: The competing effects of stability and humidity on subtropical stratocumulus entrainment and cloud evolution from a Lagrangian perspective. *J. Atmos. Sci.*, **75**, 2563–2578, https://doi.org/10.1175/JAS-D-18-0030.1.

Ebert, E. E., and J. A. Curry, 1992: A parameterization of ice cloud optical properties for climate models. *J. Geophys. Res.*, **97**, 3831–3836, https://doi.org/10.1029/91JD02472.

Frey, W. R., and J. E. Kay, 2018: The influence of extratropical cloud phase and amount feedbacks on climate sensitivity. *Climate Dyn.*, **50**, 3097–3116, https://doi.org/10.1007/s00382-017-3796-5.

Fu, Q., 1996: An accurate parameterization of the solar radiative properties of cirrus clouds for climate models. *J. Climate*, **9**,

2058–2082, https://doi.org/10.1175/1520-0442(1996)009<2058:AAPOTS>2.0.CO;2.

——, 2007: A new parameterization of an asymmetry factor of cirrus clouds for climate models. *J. Atmos. Sci.*, **64**, 4140–4150, https://doi.org/10.1175/2007JAS2289.1.

Gordon, N. D., and S. A. Klein, 2014: Low-cloud optical depth feedback in climate models. *J. Geophys. Res. Atmos.*, **119**, 6052–6065, https://doi.org/10.1002/2013JD021052.

Gregory, J. M., and Coauthors, 2004: A new method for diagnosing radiative forcing and climate sensitivity. *Geophys. Res. Lett.*, **31**, L03205, https://doi.org/10.1029/2003GL018747.

Grosvenor, D. P., and R. Wood, 2014: The effect of solar zenith angle on MODIS cloud optical and microphysical retrievals within marine liquid water clouds. *Atmos. Chem. Phys.*, **14**, 7291–7321, https://doi.org/10.5194/acp-14-7291-2014.

Hartmann, D. L., 2016: *Global Physical Climatology*. 2nd ed. Academic Press, 498 pp.

——, and K. Larson, 2002: An important constraint on tropical cloud–climate feedback. *Geophys. Res. Lett.*, **29**, 1951, https://doi.org/10.1029/2002GL015835.

Hawcroft, M., J. M. Haywood, M. Collins, A. Jones, A. C. Jones, and G. Stephens, 2017: Southern Ocean albedo, inter-hemispheric energy transports and the double ITCZ: Global impacts of biases in a coupled model. *Climate Dyn.*, **48**, 2279–2295, https://doi.org/10.1007/s00382-016-3205-5.

Haynes, J. M., C. Jakob, W. B. Rossow, G. Tselioudis, and J. Brown, 2011: Major characteristics of Southern Ocean cloud regimes and their effects on the energy budget. *J. Climate*, **24**, 5061–5080, https://doi.org/10.1175/2011JCLI4052.1.

Hersbach, H., and Coauthors, 2020: The ERA5 global reanalysis. *Quart. J. Roy. Meteor. Soc.*, **146**, 1999–2049, https://doi.org/10.1002/qj.3803.

Hu, Y. X., and K. Stamnes, 1993: An accurate parameterization of the radiative properties of water clouds suitable for use in climate models. *J. Climate*, **6**, 728–742, https://doi.org/10.1175/1520-0442(1993)006<0728:AAPOTR>2.0.CO;2.

Huang, Y., S. T. Siems, M. J. Manton, D. Rosenfeld, R. Marchand, G. M. McFarquhar, and A. Protat, 2016: What is the role of sea surface temperature in modulating cloud and precipitation properties over the Southern Ocean? *J. Climate*, **29**, 7453–7476, https://doi.org/10.1175/JCLI-D-15-0768.1.

Hwang, Y. T., and D. M. W. Frierson, 2013: Link between the double-Intertropical Convergence Zone problem and cloud biases over the Southern Ocean. *Proc. Natl. Acad. Sci. USA*, **110**, 4935–4940, https://doi.org/10.1073/pnas.1213302110.

Jeevanjee, N., and S. Fueglistaler, 2020: Simple spectral models for atmospheric radiative cooling. *J. Atmos. Sci.*, **77**, 479–497, https://doi.org/10.1175/JAS-D-18-0347.1.

Kay, J. E., C. J. Wall, V. Yettella, B. Medeiros, C. Hannay, P. Caldwell, and C. Bitz, 2016: Global climate impacts of fixing the Southern Ocean shortwave radiation bias in the Community Earth System Model (CESM). *J. Climate*, **29**, 4617–4636, https://doi.org/10.1175/JCLI-D-15-0358.1.

Kokhanovsky, A., 2004: Optical properties of terrestrial clouds. *Earth-Sci. Rev.*, **64**, 189–241, https://doi.org/10.1016/S0012-8252(03)00042-4.

Liu, Y., S. A. Ackerman, B. C. Maddux, J. R. Key, and R. A. Frey, 2010: Errors in cloud detection over the Arctic using a satellite imager and implications for observing feedback mechanisms. *J. Climate*, **23**, 1894–1907, https://doi.org/10.1175/2009JCLI3386.1.

Loeb, N. G., and Coauthors, 2018: Clouds and the Earth's Radiant Energy System (CERES) Energy Balanced and Filled (EBAF) Top-of-Atmosphere (TOA) edition-4.0 data product. *J. Climate*, **31**, 895–918, https://doi.org/10.1175/JCLI-D-17-0208.1.

Lutsko, N. J., and T. W. Cronin, 2018: Increase in precipitation efficiency with surface warming in radiative-convective equilibrium. *J. Adv. Model. Earth Syst.*, **10**, 2992–3010, https://doi.org/10.1029/2018MS001482.

——, M. Popp, R. H. Nazarian, and A. L. Albright, 2021: Emergent constraints on regional cloud feedbacks. *Geophys. Res. Lett.*, **48**, e2021GL092934, https://doi.org/10.1029/2021GL092934.

Mace, G. G., A. Protat, and S. Benson, 2021a: Mixed-phase clouds over the Southern Ocean as observed from satellite and surface based lidar and radar. *J. Geophys. Res. Atmos.*, **126**, e2021JD034569, https://doi.org/10.1029/2021JD034569.

——, and Coauthors, 2021b: Southern Ocean cloud properties derived from CAPRICORN and MARCUS data. *J. Geophys. Res. Atmos.*, **126**, e2020JD033368, https://doi.org/10.1029/2020JD033368.

Maddux, B. C., S. A. Ackerman, and S. Platnick, 2010: Viewing geometry dependencies in MODIS cloud products. *J. Atmos. Oceanic Technol.*, **27**, 1519–1528, https://doi.org/10.1175/2010JTECHA1432.1.

Marchant, B., S. Platnick, K. Meyer, G. T. Arnold, and J. Riedi, 2016: MODIS Collection 6 shortwave-derived cloud phase classification algorithm and comparisons with CALIOP. *Atmos. Meas. Tech.*, **9**, 1587–1599, https://doi.org/10.5194/amt-9-1587-2016.

McCoy, D. T., D. L. Hartmann, and D. P. Grosvenor, 2014a: Observed Southern Ocean cloud properties and shortwave reflection. Part I: Calculation of SW flux from observed cloud properties. *J. Climate*, **27**, 8836–8857, https://doi.org/10.1175/JCLI-D-14-00287.1.

——, ——, and ——, 2014b: Observed Southern Ocean cloud properties and shortwave reflection. Part II: Phase changes and low cloud feedback. *J. Climate*, **27**, 8858–8868, https://doi.org/10.1175/JCLI-D-14-00288.1.

Mitchell, J., C. Senior, and W. Ingram, 1989: CO_2 and climate: A missing feedback? *Nature*, **341**, 132–134, https://doi.org/10.1038/341132a0.

Mülmenstädt, J., and Coauthors, 2021: An underestimated negative cloud feedback from cloud lifetime changes. *Nat. Climate Change*, **11**, 508–513, https://doi.org/10.1038/s41558-021-01038-1.

Myers, T. A., R. C. Scott, M. D. Zelinka, S. A. Klein, J. R. Norris, and P. M. Caldwell, 2021: Observational constraints on low cloud feedback reduce uncertainty of climate sensitivity. *Nat. Climate Change*, **11**, 501–507, https://doi.org/10.1038/s41558-021-01039-0.

Norris, J. R., and S. F. Iacobellis, 2005: North Pacific cloud feedbacks inferred from synoptic-scale dynamic and thermodynamic relationships. *J. Climate*, **18**, 4862–4878, https://doi.org/10.1175/JCLI3558.1.

Petty, G. W., 2006: *A First Course in Atmospheric Radiation*. 2nd ed. Sundog Publishing, 459 pp.

Platnick, S., and Coauthors, 2017: The MODIS cloud optical and microphysical products: Collection 6 updates and examples from Terra and Aqua. *IEEE Trans. Geosci. Remote Sens.*, **55**, 502–525, https://doi.org/10.1109/TGRS.2016.2610522.

Sagan, C., and J. B. Pollack, 1967: Anisotropic nonconservative scattering and the clouds of Venus. *J. Geophys. Res.*, **72**, 469–477, https://doi.org/10.1029/JZ072i002p00469.

Sassen, K., Z. Wang, and D. Liu, 2008: Global distribution of cirrus clouds from CloudSat/Cloud-Aerosol Lidar and Infrared

Pathfinder Satellite Observations (CALIPSO) measurements. *J. Geophys. Res.*, **113**, D00A12, https://doi.org/10.1029/2008JD009972.

Scott, R. C., T. A. Myers, J. R. Norris, M. D. Zelinka, S. A. Klein, M. Sun, and D. R. Doelling, 2020: Observed sensitivity of low-cloud radiative effects to meteorological perturbations over the global oceans. *J. Climate*, **33**, 7717–7734, https://doi.org/10.1175/JCLI-D-19-1028.1.

Sherwood, S. C., and Coauthors, 2020: An assessment of Earth's climate sensitivity using multiple lines of evidence. *Rev. Geophys.*, **58**, e2019RG000678, https://doi.org/10.1029/2019RG000678.

Shupe, M. D., and Coauthors, 2008: A focus on mixed-phase clouds. *Bull. Amer. Meteor. Soc.*, **89**, 1549–1562, https://doi.org/10.1175/2008BAMS2378.1.

Stackhouse, P. W., Jr., and G. L. Stephens, 1991: A theoretical and observational study of the radiative properties of cirrus: Results from FIRE 1986. *J. Atmos. Sci.*, **48**, 2044–2059, https://doi.org/10.1175/1520-0469(1991)048<2044:ATAOSO>2.0.CO;2.

Storelvmo, T., I. Tan, and A. V. Korolev, 2015: Cloud phase changes induced by CO_2 warming—A powerful yet poorly constrained cloud-climate feedback. *Curr. Climate Change Rep.*, **1**, 288–296, https://doi.org/10.1007/s40641-015-0026-2.

Tan, I., T. Storelvmo, and M. D. Zelinka, 2016: Observational constraints on mixed-phase clouds imply higher climate sensitivity. *Science*, **352**, 224–227, https://doi.org/10.1126/science.aad5300.

——, L. Oreopoulos, and N. Cho, 2019: The role of thermodynamic phase shifts in cloud optical depth variations with temperature. *Geophys. Res. Lett.*, **46**, 4502–4511, https://doi.org/10.1029/2018GL081590.

Terai, C. R., M. D. Zelinka, and S. A. Klein, 2016: Constraining the low-cloud optical depth feedback at middle and high latitudes using satellite observations. *J. Geophys. Res. Atmos.*, **121**, 9696–9716, https://doi.org/10.1002/2016JD025233.

——, Y. Zhang, S. A. Klein, M. D. Zelinka, J. C. Chiu, and Q. Min, 2019: Mechanisms behind the extratropical stratiform low-cloud optical depth response to temperature in ARM site observations. *J. Geophys. Res. Atmos.*, **124**, 2127–2147, https://doi.org/10.1029/2018JD029359.

Thompson, D. W. J., S. Bony, and Y. Li, 2017: Thermodynamic constraint on the depth of the global tropospheric circulation. *Proc. Natl. Acad. Sci. USA*, **114**, 8181–8186, https://doi.org/10.1073/pnas.1620493114.

Trenberth, K. E., and J. T. Fasullo, 2010: Simulation of present-day and twenty-first-century energy budgets of the Southern Oceans. *J. Climate*, **23**, 440–454, https://doi.org/10.1175/2009JCLI3152.1.

Tselioudis, G., W. B. Rossow, and D. Rind, 1992: Global patterns of cloud optical thickness variation with temperature. *J. Climate*, **5**, 1484–1495, https://doi.org/10.1175/1520-0442(1992)005<1484:GPOCOT>2.0.CO;2.

——, A. D. Del Genio, W. Kovari Jr., and M. Yao, 1998: Temperature dependence of low cloud optical thickness in the GISS GCM: Contributing mechanisms and climate implications. *J. Climate*, **11**, 3268–3281, https://doi.org/10.1175/1520-0442(1998)011<3268:TDOLCO>2.0.CO;2.

Tsushima, Y., and Coauthors, 2006: Importance of the mixed-phase cloud distribution in the control climate for assessing the response of clouds to carbon dioxide increase: A multi-model study. *Climate Dyn.*, **27**, 113–126, https://doi.org/10.1007/s00382-006-0127-7.

Wall, C. J., D. L. Hartmann, and P. Ma, 2017: Instantaneous linkages between clouds and large-scale meteorology over the Southern Ocean in observations and a climate model. *J. Climate*, **30**, 9455–9474, https://doi.org/10.1175/JCLI-D-17-0156.1.

Wood, R., and C. S. Bretherton, 2006: On the relationship between stratiform low cloud cover and lower-tropospheric stability. *J. Climate*, **19**, 6425–6432, https://doi.org/10.1175/JCLI3988.1.

Zelinka, M. D., S. A. Klein, and D. L. Hartmann, 2012: Computing and partitioning cloud feedbacks using cloud property histograms. Part I: Cloud radiative kernels. *J. Climate*, **25**, 3715–3735, https://doi.org/10.1175/JCLI-D-11-00248.1.

——, T. A. Myers, D. T. McCoy, S. Po-Chedley, P. M. Caldwell, P. Ceppi, S. A. Klein, and K. E. Taylor, 2020: Causes of higher climate sensitivity in CMIP6 models. *Geophys. Res. Lett.*, **47**, e2019GL085782, https://doi.org/10.1029/2019GL085782.

Zhang, D., Z. Wang, and D. Liu, 2010: A global view of midlevel liquid-layer topped stratiform cloud distribution and phase partition from CALIPSO and CloudSat measurements. *J. Geophys. Res.*, **115**, D00H13, https://doi.org/10.1029/2009JD012143.